Synthesis of Lawsonia Inermis (henna) Carbon Supported CuO nanocomposite, Characterization and Photocatalytic Activity Studies

T. Sivasankar[1], R. Naveenkumar [1], B. Karthikeyan[1*], B. Vijayakumar [2]
[1]*Department of chemistry, Annamalai university, Tamil Nadu, 608 002, India.*
[2]*Department of chemistry, Panimalar Engineering College, Tamil Nadu, 600 123, India.*
**Author for Correspondence E-mail: bkarthi_au@yahoo.com*

Abstract

For the first report, the synthesis of a henna carbon-supported CuO nanocomposite is disclosed. The co precipitation process is an excellent way to make pure CuO and C- CuO nanocomposites and it has a better photocatalytic degradation. FT-IR, P-XRD, FE-SEM, UV-DRS, and PL studies are used to assess the structural, optical, and morphological characteristics of the produced nanocomposites. The FE-SEM displays the composites' uniform distribution.

The FT-IR spectra is used to identified the CuO and C-CuO nanocomposite. According to XRD, cubic phase is present in the nanomaterials. The bandgap value of 1.81 for C-CuO and 2.46 eV for CuO, respectively, make these nanocomposites as strong semi-conductors. CuO depicts the cube-shaped, smooth-surfaced morphology, while the carbon is uniformly distributed throughout the CuO in the C-CuO nanocomposite has a rod shape. Carbon may introduce defects, excited carriers can lose their energy through these non-radiative pathways, resulting in a reduction in photoluminescence intensity. To measure the photocatalytic activity of the composites, methylene blue (MB) dye is used as a model pollutant. CuO and C-CuO catalysts' photodegradation capabilities rose to 80.79 and 92.53%, respectively. Therefore, the C-CuO combination works better than the pure CuO. Henna carbon is synthesized from henna leaves. The carbon effect is proposed as one potential mechanism along with the usual photocatalytic mechanism.

Keywords: MB dye , CuO, Henna carbon, Nanocomposite and Photocatalytic degradation.

1. Introduction

Significant efforts have been undertaken in the last several years to degrade micropollutants, which are low in concentration but have a substantial risk of inflicting severe environmental damage. These pollutants include endocrine-disrupting chemicals, persistent organic and inorganic contaminants, medicines, and more. Water is a vital resource for survival, yet there is now a shortage of drinking water due to the discharge of harmful, nonbiodegradable organic and inorganic chemical contaminants into water bodies. With the growth of industries, it has turned into a threat to ecological balance, human health, and the advancement of commercial society. Almost two million tons of industrial, agricultural, and sewage waste are discharged into the water daily, causing serious health issues and over 14,000 human fatalities. Water contamination must be controlled immediately, which is why several remedies have been adopted slowly. Numerous remediation approaches have been industrialized to eliminate contaminants; nevertheless, since wastewater treatment procedures need large amounts of energy and have significant treatment costs, it remains difficult to treat effluent efficiently and economically. Coagulation, flocculation, ion exchange, adsorption, precipitation, reverse osmosis, membrane filtration, chlorination, photoelectrochemistry,

sedimentation, neutralization and other conventional techniques have all been used in the past. These conventional methods have several drawbacks. For instance, extra chemicals that can be dangerous are required for the procedures of flocculation and coagulation, which are used to remove insoluble materials from water. Surplus anions and cations are also eliminated via membrane filtering and reverse osmosis, although these processes often leave behind organic pollutants and solvents (such as benzene, insecticides, and phenolic and halogenated compounds). It should be stated that the aforementioned techniques have disadvantages, such as the need for expensive equipment, high running costs, and poor energy efficiency. Therefore, it is imperative to create innovative methods that may efficiently remove contaminants from wastewater while remaining inexpensive and ecologically beneficial [1-4].

Among these tactics are chemical oxidation, ozonolysis, ion exchange, coagulation-based, and photocatalytic degradation processes. Water contaminants may be removed by adsorption. Nonetheless, it is thought that using a semiconductor photocatalyst for photocatalytic degradation provides an economical and environmentally friendly method of effectively degrading dyes [5–19].

The four primary methods now being explored to guarantee a decent degree of control over the characteristics and performance of industrial-scale catalysts are impregnation, hydrothermal approach and deposition–precipitation. Fusing and solid-state reactions are two other techniques that may be used. However, a considerable amount of solvent waste is always produced by solution-based procedures due to their inherent nature. Furthermore, metal salts such as nitrate or chloride are often utilized as precursors, which may result in the production of hazardous vapors during the subsequent calcination operations. It could be necessary to take the necessary steps to stop these gasses from leaking into the atmosphere [20–22].

One important class of transition metal oxides is represented by copper oxides. One of the two stable oxides of copper, the other being Cu_2O (cuprous oxide), is cupric oxide (CuO), also known by the mineral name tenorite. CuO is a black solid. CuO exhibits a monoclinic unit cell with space group C_2/c, where four oxygen atoms coordinate with each Cu atom. With a band gap of 1.2 eV, CuO is a significant, inexpensive, and nontoxic p-type semiconductor material. Due to CuO's many uses in gas sensors, biosensors, photo-detectors, magnetic storage media, supercapacitors, photocatalysis, removal of inorganic pollutants, and antimicrobial applications, knowledge of its physical and chemical characteristics is of great interest [23].

A cationic dye called methylene blue (MB) is often used in the production of silk garments. It is thought to be carcinogenic and mutagenic, and it possesses hazardous qualities for many kinds of life. In addition, the textile, paper, rubber, plastic, printing, and dyeing sectors also create MB-contaminated effluents. Its structure is stable, making it difficult for it to biodegrade. As a result, there is an increased need to create effective remediation solutions to remove such toxic dyes [24–25].

To the best of our knowledge, co-precipitation method was used in the synthesis of pure CuO and C-CuO nanocomposite and produced carbon from the leaf of Lawsonia inermis, often known as henna. Characterization of the nanocomposite is accomplished by the use of FT-IR, P-XRD, FE-SEM, UV-DRS, and PL analysis. We assessed the catalysts efficiency in photodegradation is also presented in detail.

2. Experimental methods

2.1 Materials

Henna leaves were collected from the Annamalai university campus. Whatman filter paper, NaOH, EtOH, copper chloride ($CuCl_2$), distilled water. All chemicals acquired from OTTO chemicals, Mumbai and all aqueous solution was make using distilled water.

2.2 Henna carbon synthesis from henna leaf

20g of the leaves were thoroughly cleansed with deionized water to remove any dust, and they were left to dry for a week at room temperature. After that, the sample was put in an alumina crucible and dried in a vacuum oven for five hours at 90^0C. Taken the samples were cooled naturally for three hours. Finally, the prepared carbon samples were collected for the characterization.

2.3 Henna leaf extract extraction

To remove filth, refreshing henna leaves were continuously washed with distilled water. To achieve the perfect amount of dryness, the leaves were then allowed to air dry for five days at room temperature. After that, a mortar and pestle were used to grind it into a fine powder. Ten grams of the powdered henna leaf were added with 200 mL of distilled water boiled to create henna leaf extract. The mixture was heated to 80^0C for 90 minutes. The solution was allowed to grad cool to room temperature before being filtered through Whatman Grade 1 filter paper and kept cold (at 5 °C) to keep it fresh for later use.

2.4 Synthesis of C-CuO nanocomposite

After dissolving 0.2 M $CuCl_2$ solution in 100mL of distilled water and magnetically stirring for 20 minutes at 85^oC, 30mL of henna leaf extract was added, and a precipitate was produced. Next, addition of 0.1M NaOH to promote the precipitation of a dark black hue for 3 hours. Then, followed by the 0.05g of henna carbon was added and constantly stirred for 1 hour. The sample was filtered, cleaned through ethanol, and dried for three hours at 100^oC in an oven. It was then stored for 5 hours at 500^0C in a muffle furnace. The same process follows to synthetic bare CuO nanoparticles.

2.5 Studies of Characterization

The X-ray system (XPERT PRO) Cu-Kα radiation (λ = 1.5418 Å), which was used to study the diffraction characteristics of the samples. The functional groups of the materials were determined by the use of an FT-IR spectrophotometer (IR Tracer-100 Shimadzu). Diffuse reflectance spectra (UV-vis DRS) between 200 and 800 nm were found using the Shimadzu UV-2600. A Perkin Elmer LS 55 fluorescence spectrometer was used to measure the sample photoluminescence emission. The morphology of the nanocomposites was investigated using the CARL ZEISS-SIGMA 300 FESEM with the EDAX FE-SEM apparatus model.

2.6 Photocatalytic study

The photocatalytic activity of the produced CuO and C-CuO nanocomposites was investigated via MB dye. A 0.001M dye solution containing 0.1g of the photocatalyst was used to individually photocatalyst the breakdown of MB in 100 mL of clean water. The solution was exposed to under UV radiation in the photoreactor chamber, and samples remained collected at regular 15-minutes breaks. A UV-visible spectrophotometer with a wavelength range of 200 to 800 nm was used to assess the deterioration. The wavelength at which MB dye absorbs was determined to be 665 nm.

$$\text{Degradation Rate (\%)} = \frac{Co-Ct}{c_0} \times 100 \qquad (1)$$

Where, Ct is the concentration of the MB after a certain amount of time, and C_0 is the concentration of the MB at the start.

3. Result and discussion

3.1 FT-IR analysis

The FT-IR spectra of the C-CuO nanocomposite and the produced CuO NPs, as shown in Figure 1(a,b), indicated the existence of primary peaks at the broad bands at 3400-3600 cm^{-1}, corresponding to the O-H bond asymmetric stretching vibration. This is due to the fact that every distinct chemical link often has a distinct energy absorption band. In order to

examine the kind and strength of bonding, it may also be used to gather structural and bond information about a complex. Different types of bending vibration of the Cu–O bond is shown by the existence of bands at 523 cm^{-1}, 1011 cm^{-1}, 624, and 844 cm^{-1}. The peak's appearance at 1639 cm^{-1} suggests that the Cu–O link in copper (II) oxide nanoparticles is stretching. Furthermore, at 624 cm^{-1}, the existence of CuO's distinctive vibrational peak is noted [26–28]. Finally, it has been shown that doping tends to decrease particle size, as seen by the growing and broadening of the IR band upon exposure of CuO to more carbon shown in Figure 1(b). The system experiences local lattice distortions and defects as the particle size reduces, which weakens the crystal symmetry and enlarges the FT-IR peaks.

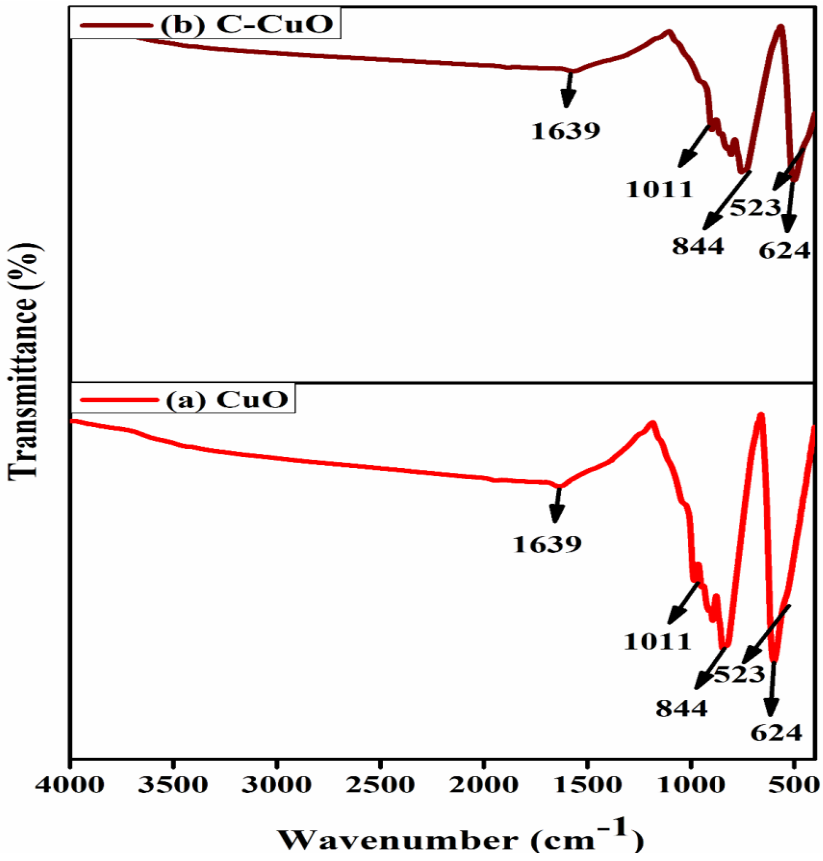

Figure. 1 FT-IR spectra of the synthesized a) CuO, b) C-CuO nanocomposite

3.2 P-XRD analysis

Using X-ray diffraction, the structural analysis of both C-CuO and virgin CuO nanoparticles has been completed. Patterns of X-ray diffraction (XRD) are shown in Figure 2, Figure 2 (a) show the synthesized CuO sample is in monoclinic phase. The XRD patterns indicated diffraction peaks (110), (111), (211), (202), (020), (202), (022), (113), (202), (311), and (004) match with the standard diffraction peaks (JCPDS: card no. 48-1548) rather well. The (111) and (111) peaks have substantially greater intensities than the other peaks, indicating that these orientations are where the produced nanocrystals prefer to be oriented. Additionally, no impurity peak was seen in the XRD patterns. The monoclinic structure of CuO diffraction data (JCPDS card no. 48-1548) is consistent with the well-defined diffraction peaks [29, 30]. Based on the discovered low-intensity peaks for C-CuO, the produced CuO sample is largely composed of CuO nanocomposite is shown in Figure 2 (b). The intensity was lower if the C-CuO, the carbon may be disordered or amorphous. This may lead to an absence of distinct peaks.

$$D = \frac{0.98\lambda}{\beta Cos\theta} \qquad (2)$$

Where, D is the crystalline size, β is the full-width half maximum calculated from the peak of greatest intensity, λ is the wavelength of the X-ray beam operating system and θ is the diffraction angle. The average crystalline size of the CuO and C-CuO nanocomposite were determined to be 10.26 nm and 8.63 nm, respectively, using equation 2 of the Debye-Scherrer formula.

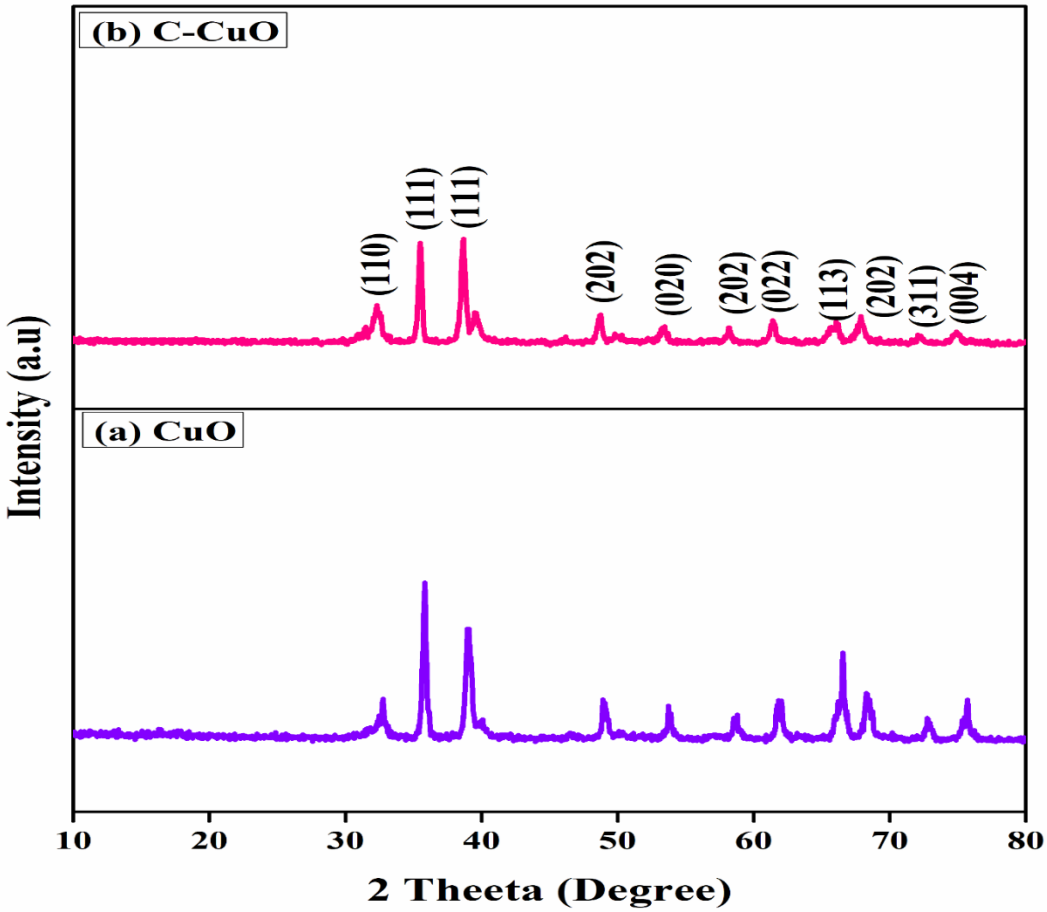

Figure. 2 XRD pattern of a) CuO, b) C-CuO nanocomposite

3.3 FE-SEM analysis

As shown in Figure 3(a and b), the surface morphology of the CuO NPs and C-CuO nanocomposite was investigated using field emission scanning electron microscopy. Figure 3(a) depicts the cube-shaped, smooth-surfaced morphologies of the as-prepared CuO NPs. While the carbon is uniformly distributed throughout the CuO in Figure 3(b), the C-CuO nanocomposite has a rod shape. On the other hand, the CuO nanocomposite exhibits a greater particle size than the C-CuO nanocomposite. High temperatures probably had an impact on the rate of nucleation of the NPs in both pathways, which may have been caused by product supersaturation and hastened formation. The structure and morphology of the NPs may be determined by their rate of aggregation [31–33]. CuO and C-CuO nanocomposite have a mean particle size of about 54.45 and 35.41 nm, respectively, and exhibit excellent homogeneity, cube form, and suitable separation. However, some aggregates were also seen, which could have resulted from agglomeration during the washing process. The findings of energy dispersive spectroscopy (EDS) on both pure CuO and C-CuO are shown in Figure 3.

Since the only components shown in the research are the Cu, O, and C signals, EDS analysis confirmed that C-CuO is produced.

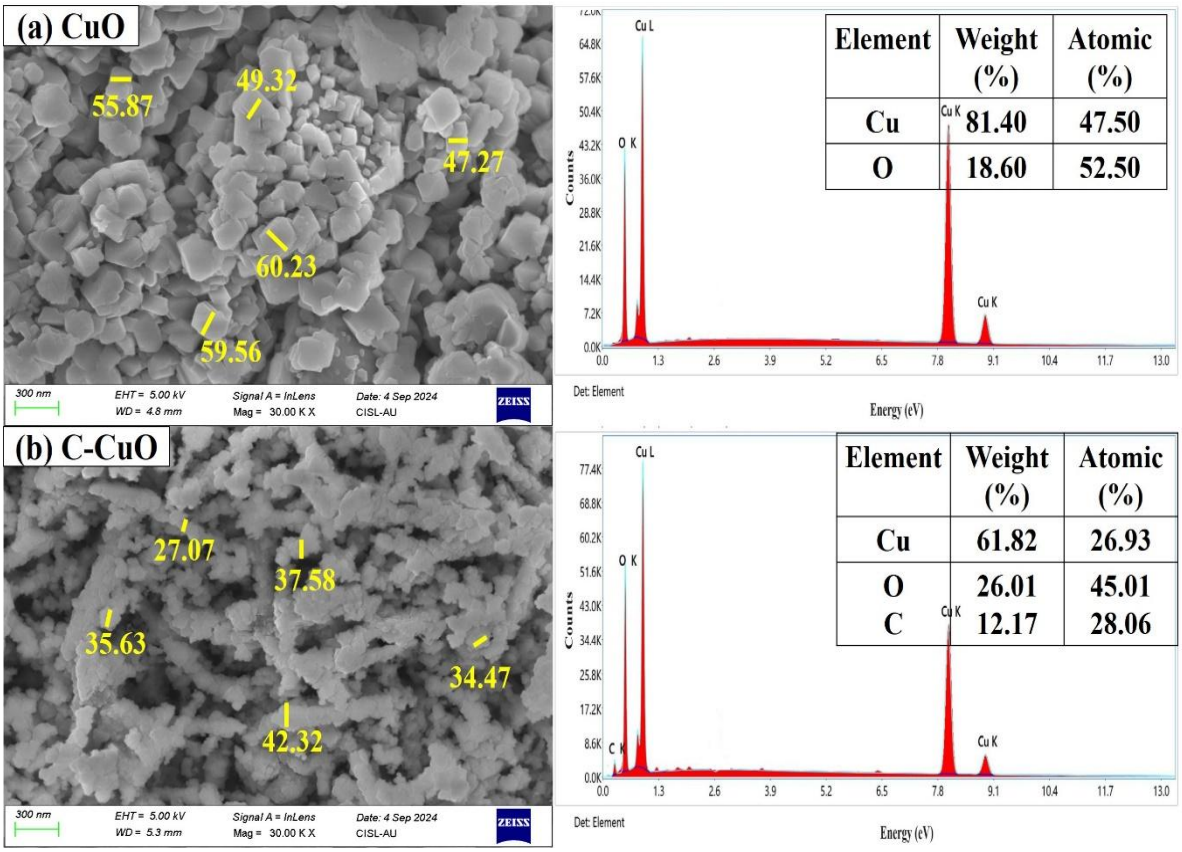

Figure. 3 FE-SEM image of a) CuO, b) C-CuO nanocomposite

3.4 UV-DRS analysis

Using UV-Vis-DRS spectra, the optical characteristics of both pure CuO and C-CuO nanocomposite were examined. Figure 4 displays the recorded DRS spectra. The diffuse reflectance spectra (DRS) are shown in Figure 4. The optical reflectance spectra were collected within the wavelength range of 200–800 nm. The well-known Kubelka-Munk relation equation (3) was used to get the band gap values of CuO and C-CuO. The calculated band gap energy values for each scenario are 2.46 and 1.81 eV (Figure. 4).

$$\alpha h\nu = A\,(h\nu - E_g)^{1/2} \qquad (3)$$

Where, n = 2 is the direct energy bandgap, A is the material constant, and Eg is the bandgap energy [34, 35]. The carbon composite in the C-CuO material clearly shows how its band gap energy is lower than that of pure CuO in Figure 4. When carbon is added, the band gap of C-CuO is less than that of pure CuO nanoparticles. Consequently, it is suggested that the C-CuO nanocomposite's lower band gap energy may be used to provide the desired photocatalytic activity.

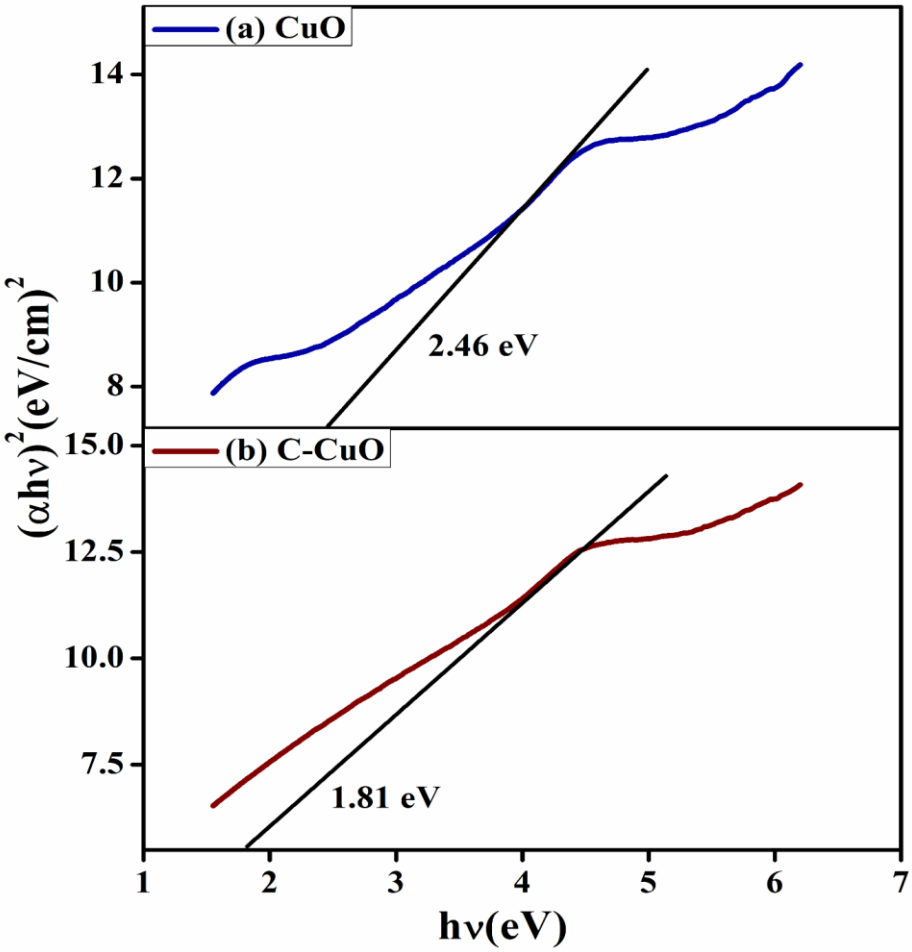

Figure .4 UV-DRS visible spectra of a) CuO, b) C-CuO nanocomposite

3.5 Photoluminescence analysis

The Figure 5 illustrates the excitation wavelength effect the photoluminescence spectra of CuO and C-CuO. Two emission peaks were seen in the photoluminescence study at 475 nm (blue) and 385 nm (violet) (Figure 5). The first one is associated with band-edge emission, whereas the second one results from artifacts. Sharp visible emission peak and a wide UV emission peak, referred to as the near band-edge emission, are present in the spectrum. The UV emission peaks in Figure 5 are associated with spectra that are situated between 360 and 390 nm. The findings of Figure 5 were obtained using an excitation wavelength of 300 nm. According to the above-calculated Eg, reveals a blue shift with decreasing nanoparticle size as a result of the narrow bandgap brought on by an increase in quantum-confinement effects. The emission seen at the band edge is ascribed to the recombination of electrons and holes of CuO-free excitons, a process that is very sensitive to particle size in quantum mechanics. Consequently, the lower intensity of the C-CuO nanocomposite in comparison to CuO indicates that electron and hole recombination is suppressed and that these particles take part in photochemical transformation, thus augmenting the photocatalytic activity of the nanocomposites.

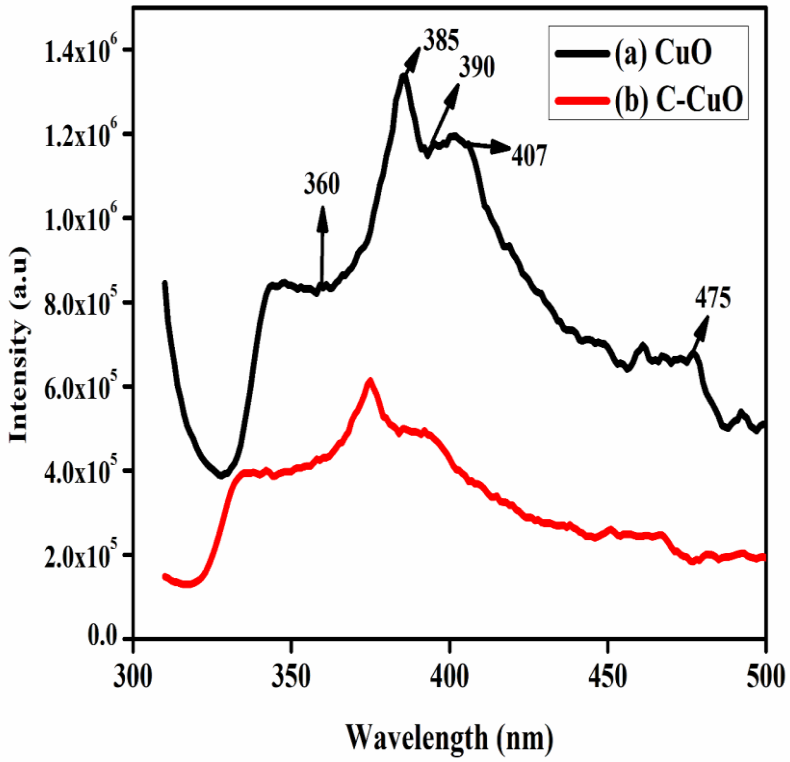

Figure .5 PL emission spectra of a) CuO, b) C-CuO nanocomposite

3.6 Photocatalytic activity studies

The nanocomposites' ability to remove MB is their photocatalytic activity is measured. A 100 mg sample of CuO and C-CuO nanocomposite was added in 100 mL (10^{-4}) of MB solution and exposed to UV light. To measure photocatalytic activity, 3 mL of the MB solution is taken out of the dye solution every 15 minutes. Figure 6 shows the measurement of MB dye absorption at a wavelength of 665 nm. Equation (1) was used to compute the degradation rate % in this manner. Where Ct denotes the initial dye solution concentration (mg L^{-1}) and C_0 denotes the ultimate dye solution concentration (mg L^{-1}) at a certain time point.

Figure 7(a,b) displays the photocatalytic activity of the CuO and C-CuO nanocomposites. C-CuO nanocomposites have greatly more photocatalytic activity compared with CuO NPs. After 15 minutes of exposure to UV radiation, MB is entirely photodegraded by C-CuO nanocomposites. This highlights the critical role that transparency plays in MB photodegradation. The photocatalytic activity rises with the concentration of henna carbon. Figure 7 (a,b) illustrates the MB dye degradation on the catalyst surface during 120 minutes. The concentration of the MB dye decreases with increasing time intervals.

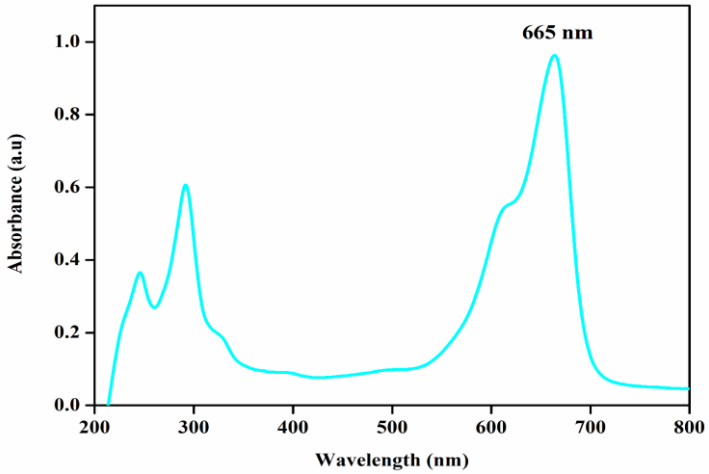

Figure .6 UV-Visible absorption spectrum of MB dye

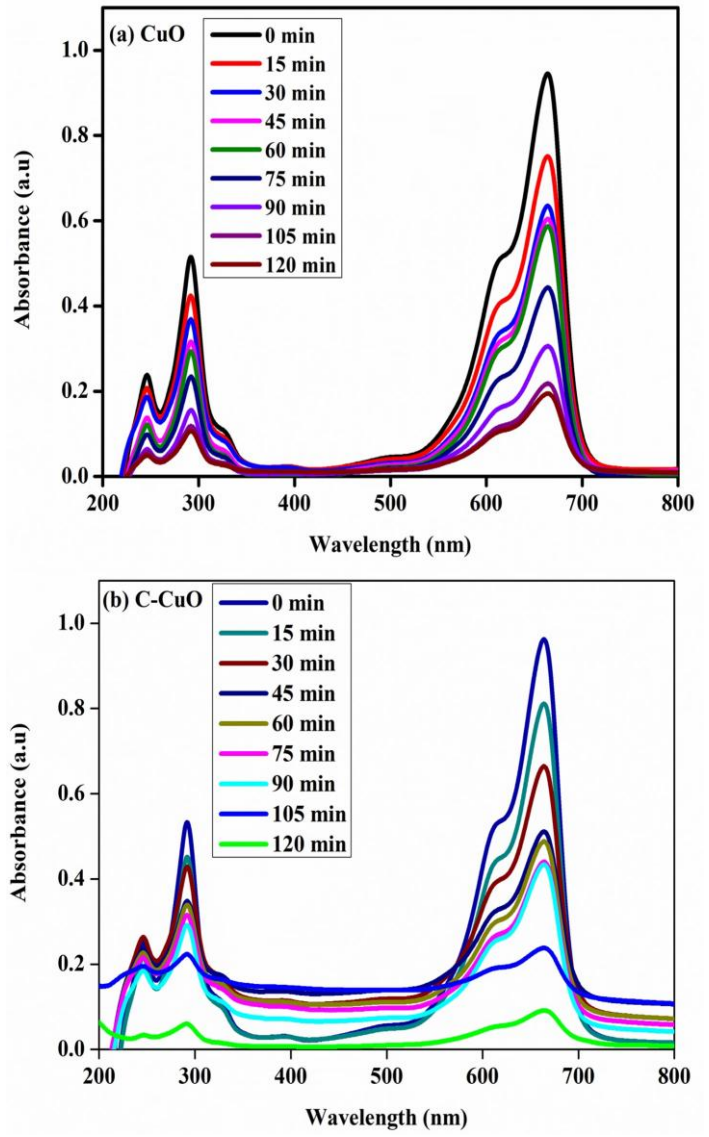

Figure .7 Photodegradation spectrum of MB dye under UV-light a) CuO, b) C-CuO nanocomposite

The fundamental reason of the photocatalytic degradation pathway is explained by equation (4-9). Hydroxyl radicals blanket the catalyst surface as a result of electrons migrating from the conduction band to the valence band. The hydroxyl radical produced has an impact on the dye molecule's conjugation mechanism. Furthermore, the holes will react with water to produce hydroxyl radicals, or radicals with an ·OH suffix. As has been covered in a number of papers, superoxide and radicals are the primary catalysts for the breakdown of dye molecules, which results in the production of H_2O, CO_2, and other compounds [40–46].

$$\text{C-CuO} + h\nu \rightarrow e^- + h^+ \quad (4)$$

$$H_2O + h^+ \rightarrow H^+ + {}^{\cdot}OH \quad (5)$$

$$O_2 + e^- \rightarrow {}^{\cdot}O_2^- \quad (6)$$

$$O_2^- + 2H^+ \rightarrow H_2O_2 \quad (7)$$

$${}^{\cdot}OH + \text{MB Dye} \rightarrow \text{Degraded product} \quad (8)$$

$${}^{\cdot}O_2^- + \text{MB Dye} \rightarrow CO_2 + H_2O \quad (9)$$

Figure 8 shows the proportion of MB dye degradation (%). The breakdown of the aromatic rings in the MB dye molecule reduces the absorbance of the dye solution even further. After 120 minutes of UV irradiation, CuO only destroys MB 80.79 %; in contrast, C-CuO composite degrades the dye to 92.53%. The rapid photodegradation of MB dye by C-CuO might be associated with a potent electron-hole dividing capability. The henna carbon effect reduces electron-hole recombination, which boosts photocatalytic activity. Comparing the C-CuO composite to the other samples, it exhibits more photocatalytic activity and a larger active surface area. Their investigation revealed that the prevention of electron-hole pair recombination promoted the activation of the active radical species, which in turn accelerated dye degradation when UV light stimulated CuO nanoparticles supported by carbon.

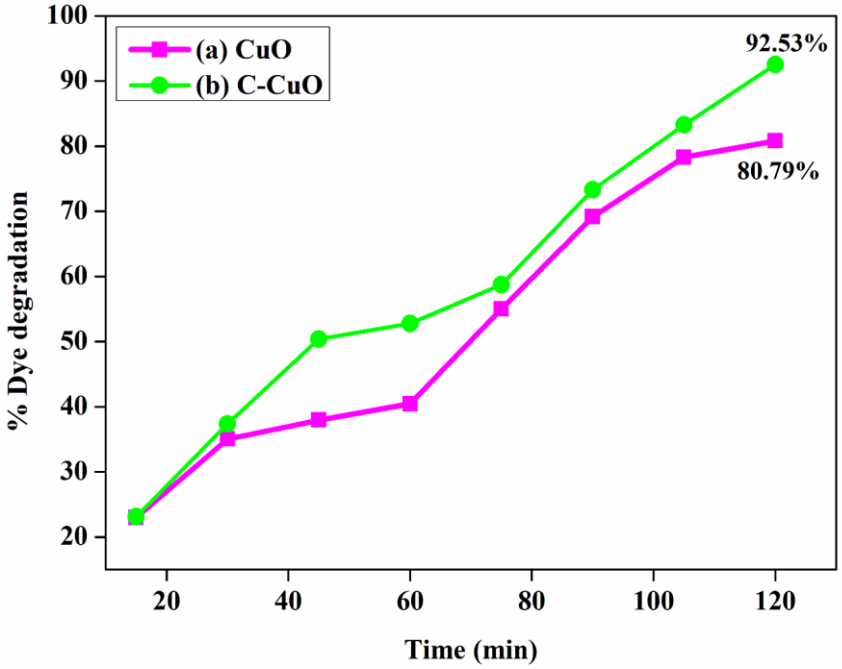

Figure.8 Degradation % of a) CuO, b) C-CuO nanocomposites

3.7 Study of kinetics

Equation (10) shows that the photodegradation of MB dye with a photocatalyst often occurs in pseudo-first order.

$$\ln (C_0 / C_t) = kt \quad (10)$$

Where kt is the rate constant (min), C_0 is the initial dye concentration, at reaction time (t), and Ct is the final dye concentration at that end time. Figure 9 (a & b) displays a plot of the time-dependent UV light irradiation, photodegradation rate, and photocatalyst efficiency for the photocatalyst samples. The graph shows the C-CuO nanocomposite's dynamic efficiency of MB dye degradation after a pseudo-first-order request response rate.

The linear connection between the slopes of the curves shows that the k values for pure CuO and C-CuO are 0.0138 and 0.0222, respectively. CuO's R^2 value is 0.9648, whereas C-CuO's is 0.975. Based on the rate constant values, the C-CuO shows improved dye degradation efficiency in 9 (a& b).

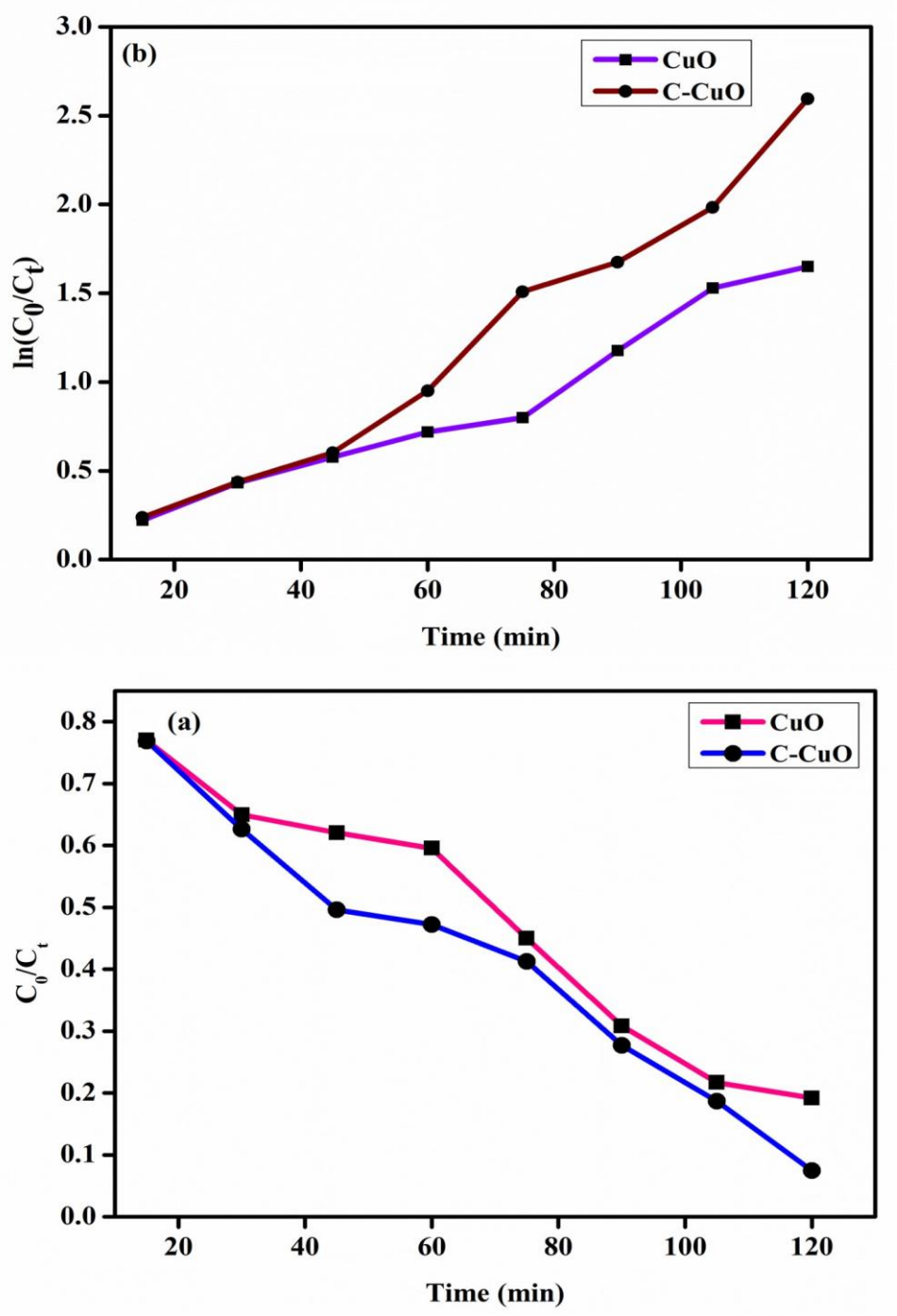

Figure .9 (a &b) Kinetic graph of a) CuO, b) C-CuO.

4.Conclusion

This work successfully produced henna carbon, which was then used to synthesize pure CuO and C-CuO. Utilizing FT-IR, P-XRD, FE-SEM, UV-DRS, and PL, the produced composites were examined. MB dye is used to assess the photocatalytic activity of the photocatalyst. The functional group of the chemical bond structure of the composites were determined by the application of FT-IR data. The XRD investigation indicates that the materials used in composites have various characteristics. The uniform distribution of the composites was shown by the FE-SEM data. The constituents of composites have been ascertained by the outcomes of an EDS analysis. An MB dye deteriorated by 80.79% in 120 minutes by CuO, whereas C-CuO demonstrated a degradation efficiency of 92.53%. It was discovered that the effectiveness of MB breakdown is added by henna carbon. When compared to CuO, C-CuO material has superior photocatalytic capabilities. The results imply that these C-CuO might be helpful as potential photocatalysts in the dye pollution photodegradation process.

Acknowledgement

None

Author contribution

T. Sivasankar contributed in collect primary data, Design the Experiment, do the experimental analysis and overall manuscript writing and finalizing it. R. Naveen kumar, B. Karthikeyan, and B. Vijayakumar, were involved in supervision, formal analysis, contribute in draft, check draft, resources and editing manuscript and provided necessary facilities.

Conflict of interest statement

The authors declare no conflict of interest in this research work.

Data availability statement

Manuscript has no associated data.

5.References

1. Abaker M, Umar A, Baskoutas S, Kim SH, Hwang SW. Structural and optical properties of CuO layered hexagonal discs synthesized by a low-temperature hydrothermal process. Journal of Physics D: Applied Physics. 2011 Mar 28;44(15):155405.
2. Ahmad F, Agusta MK, Dipojono HK. Electronic and optical properties of CuO based on DFT+ U and GW approximation. InJournal of Physics: Conference Series 2016 Aug 1 (Vol. 739, No. 1, p. 012040). IOP Publishing.
3. Ahmed S, Rasul MG, Brown R, Hashib MA. Influence of parameters on the heterogeneous photocatalytic degradation of pesticides and phenolic contaminants in wastewater: a short review. Journal of environmental management. 2011 Mar 1;92(3):311-30.
4. Alishah H, Pourseyedi S, Ebrahimipour SY, Mahani SE, Rafiei N. Green synthesis of starch-mediated CuO nanoparticles: preparation, characterization, antimicrobial activities and in vitro MTT assay against MCF-7 cell line. Rendiconti Lincei. 2017 Mar;28:65-71.
5. Ahmad A, Mohd-Setapar SH, Chuong CS, Khatoon A, Wani WA, Kumar R, Rafatullah M. Recent advances in new generation dye removal technologies: novel search for approaches to reprocess wastewater. RSC advances. 2015;5(39):30801-18.
6. Piaskowski K, Świderska-Dąbrowska R, Zarzycki PK. Dye removal from water and wastewater using various physical, chemical, and biological processes. Journal of AOAC International. 2018 Sep 1;101(5):1371-84.

7. Kumar PS, Joshiba GJ, Femina CC, Varshini P, Priyadharshini S, Karthick MA, Jothirani R. A critical review on recent developments in the low-cost adsorption of dyes from wastewater. Desalination and Water Treatment. 2019 Dec 1;172:395-416.
8. Adane T, Adugna AT, Alemayehu E. Textile industry effluent treatment techniques. Journal of Chemistry. 2021;2021(1):5314404.
9. Ejraei A, Aroon MA, Saravani AZ. Wastewater treatment using a hybrid system combining adsorption, photocatalytic degradation and membrane filtration processes. Journal of Water Process Engineering. 2019 Apr 1;28:45-53.
10. Rao S, AS S, Jayaprakash GK, Swamy MM, K S, Kumar D. Plant seed extract assisted, eco- synthesized C- ZnO nanoparticles: Characterization, chromium (VI) ion adsorption and kinetic studies. Luminescence. 2023 Jul;38(7):1123-31.
11. Carabineiro SA, Thavorn-Amornsri T, Pereira MF, Figueiredo JL. Adsorption of ciprofloxacin on surface-modified carbon materials. Water research. 2011 Oct 1;45(15):4583-91.
12. Carabineiro SA, Thavorn-Amornsri T, Pereira MF, Serp P, Figueiredo JL. Comparison between activated carbon, carbon xerogel and carbon nanotubes for the adsorption of the antibiotic ciprofloxacin. Catalysis Today. 2012 Jun 1;186(1):29-34.
13. Silva AR, Martins PM, Teixeira S, Carabineiro SA, Kuehn K, Cuniberti G, Alves MM, Lanceros-Mendez S, Pereira L. Ciprofloxacin wastewater treated by UVA photocatalysis: Contribution of irradiated TiO 2 and ZnO nanoparticles on the final toxicity as assessed by Vibrio fischeri. Rsc Advances. 2016;6(98):95494-503.
14. Chakraborty R, Asthana A, Singh AK, Yadav S, Susan MA, Carabineiro SA. Intensified elimination of aqueous heavy metal ions using chicken feathers chemically modified by a batch method. Journal of Molecular Liquids. 2020 Aug 15;312:113475.
15. Yadav S, Asthana A, Chakraborty R, Jain B, Singh AK, Carabineiro SA, Susan MA. Cationic dye removal using novel magnetic/activated charcoal/β-cyclodextrin/alginate polymer nanocomposite. Nanomaterials. 2020 Jan 18;10(1):170.
16. Yadav S, Asthana A, Singh AK, Chakraborty R, Vidya SS, Susan MA, Carabineiro SA. Adsorption of cationic dyes, drugs and metal from aqueous solutions using a polymer composite of magnetic/β-cyclodextrin/activated charcoal/Na alginate: Isotherm, kinetics and regeneration studies. journal of Hazardous Materials. 2021 May 5;409:124840.
17. Yadav S, Asthana A, Singh AK, Chakraborty R, Sree Vidya S, Singh A, Carabineiro SA. Methionine-functionalized graphene oxide/sodium alginate bio-polymer nanocomposite hydrogel beads: synthesis, isotherm and kinetic studies for an adsorptive removal of fluoroquinolone antibiotics. Nanomaterials. 2021 Feb 25;11(3):568.
18. Lilhare S, Mathew SB, Singh AK, Carabineiro SA. Calcium alginate beads with entrapped iron oxide magnetic nanoparticles functionalized with methionine—A versatile adsorbent for arsenic removal. Nanomaterials. 2021 May 20;11(5):1345.
19. Martins PM, Santos B, Salazar H, Carabineiro SA, Botelho G, Tavares CJ, Lanceros-Mendez S. Multifunctional hybrid membranes for photocatalytic and adsorptive removal of water contaminants of emerging concern. Chemosphere. 2022 Apr 1;293:133548.
20. Bravo-Suárez JJ, Chaudhari RV, Subramaniam B. Design of heterogeneous catalysts for fuels and chemicals processing: An overview. Novel materials for catalysis and fuels processing. 2013:3-68.
21. Amrute AP, De Bellis J, Felderhoff M, Schüth F. Mechanochemical synthesis of catalytic materials. Chemistry–A European Journal. 2021 Apr 21;27(23):6819-47.
22. Tsuzuki T. Mechanochemical synthesis of metal oxide nanoparticles. Communications Chemistry. 2021 Oct 12;4(1):143.

23. Said MI, Othman AA. Structural, optical and photocatalytic properties of mesoporous CuO nanoparticles with tunable size and different morphologies. RSC advances. 2021;11(60):37801-13.
24. Janoš P, Buchtová H, Rýznarová M. Sorption of dyes from aqueous solutions onto fly ash. Water research. 2003 Dec 1;37(20):4938-44.
25. Seshadri S, Bishop PL, Agha AM. Anaerobic/aerobic treatment of selected azo dyes in wastewater. Waste Management. 1994 Jan 1;14(2):127-37.
26. Mohamed EA. Green synthesis of copper & copper oxide nanoparticles using the extract of seedless dates. Heliyon. 2020 Jan 1;6(1).
27. Matei A, Craciun G, Romanitan C, Pachiu C, Tucureanu V. Biosynthesis and Characterization of Copper Oxide Nanoparticles. Engineering Proceedings. 2023 May 17;37(1):54.
28. Raul PK, Senapati S, Sahoo AK, Umlong IM, Devi RR, Thakur AJ, Veer V. CuO nanorods: a potential and efficient adsorbent in water purification. Rsc Advances. 2014;4(76):40580-7.
29. Siddiqui H, Parra MR, Qureshi MS, Malik MM, Haque FZ. Studies of structural, optical, and electrical properties associated with defects in sodium-doped copper oxide (CuO/Na) nanostructures. Journal of materials science. 2018 Jun;53(12):8826-43.
30. Peng F, Sun Y, Lu Y, Yu W, Ge M, Shi J, Cong R, Hao J, Dai N. Studies on sensing properties and mechanism of CuO nanoparticles to H2S gas. Nanomaterials. 2020 Apr 17;10(4):774.
31. Okpara EC, Ogunjinmi OE, Oyewo OA, Fayemi OE, Onwudiwe DC. Green synthesis of copper oxide nanoparticles using extracts of Solanum macrocarpon fruit and their redox responses on SPAu electrode. Heliyon. 2021 Dec 1;7(12).
32. Eslami A, Juibari NM, Hosseini SG, Abbasi M. Synthesis and characterization of CuO nanoparticles by the chemical liquid deposition method and investigation of its catalytic effect on the thermal decomposition of ammonium perchlorate. Central European Journal of Energetic Materials. 2017;14(1):152-68.
33. Zhou Q, Zhang Y, Zeng T, Wan Q, Yang N. Morphology-dependent sensing performance of CuO nanomaterials. Analytica Chimica Acta. 2021 Aug 1;1171:338663.
34. Botsa SM, Basavaiah K. Removal of Nitrophenols from wastewater by monoclinic CuO/RGO nanocomposite. Nanotechnology for Environmental Engineering. 2019 Dec;4:1-7.
35. Ramya S, Viruthagiri G, Gobi R, Shanmugam N, Kannadasan N. Synthesis and characterization of Ni 2+ ions incorporated CuO nanoparticles and its application in antibacterial activity. Journal of Materials Science: Materials in Electronics. 2016 Mar;27:2701-11.
36. Troudi B, Halimi O, Sebais M, Boudine B, Djebli A. Synthesis, structural and optical properties of CuO nanocrystals embedded in polyvinyl chloride (PVC) thin films. Int. J. Mech. Prod. Eng. 2017;5(2):115-9.
37. Tamuly, C., Saikia, I., Hazarika, M., & Das, M. R. (2014). Reduction of aromatic nitro compounds catalyzed by biogenic CuO nanoparticles. *RSC Advances*, *4*(95), 53229-53236.
38. Dagher S, Haik Y, Ayesh AI, Tit N. Synthesis and optical properties of colloidal CuO nanoparticles. Journal of Luminescence. 2014 Jul 1;151:149-54.
39. Sihag S, Dahiya R, Rani S, Jatrana A, Kumar A, Kumar V. Investigation of structural and optical characteristics of CuO nanoparticles calcinated at various temperatures. Indian Journal of Chemical Technology (IJCT). 2022 May 9;29(5):578-82.

40. Jiang Y, Liu D, Cho M, Lee SS, Zhang F, Biswas P, Fortner JD. In situ photocatalytic synthesis of Ag nanoparticles (nAg) by crumpled graphene oxide composite membranes for filtration and disinfection applications. Environmental Science & Technology. 2016 Mar 1;50(5):2514-21.
41. Naveenkumar R, Karthikeyan B, Senthilvelan S. Synthesis of bioinspired lotus fiber infused PVA/TiO2 nanocomposites: characterization, thermal, and photocatalytic activity studies. Biomass Conversion and Biorefinery. 2023 Dec 26:1-3.
42. Kulal D, Kodialbail VS. Visible light mediated photocatalytic dye degradation using Ag2O/AgO-TiO2 nanocomposite synthesized by extracellular bacterial mediated synthesis-An eco-friendly approach for pollution abatement. Journal of Environmental Chemical Engineering. 2021 Aug 1;9(4):105389.
43. Naveenkumar R, Karthikeyan B, Senthilvelan S. Facile Green Synthesis of Activated Biocarbon-Cobalt-Doped TiO2 Nanocomposite for Enhanced Antibacterial Effect and Efficient Photocatalytic for Dye Degradation. Brazilian Journal of Physics. 2024 Oct;54(5):170.
44. Berede HT, Andoshe DM, Gultom NS, Kuo DH, Chen X, Abdullah H, Wondimu TH, Wu YN, Zelekew OA. Photocatalytic activity of the biogenic mediated green synthesized CuO nanoparticles confined into MgAl LDH matrix. Scientific Reports. 2024 Jan 28;14(1):2314.
45. Naveenkumar R, Karthikeyan B, Senthilvelan S. Photocatalytic Degradation of Toxic Rhodamine B Dye by Green- Synthesised Activated Carbon- Supported Cobalt Doped ZnO With Further Assessment of ZnO Nanoparticles in Antimicrobial Applications. ChemistrySelect. 2024 Aug 5;9(29):e202401448.
46. Vijayakumar, B., & Karthikeyan, B. (2022). Synthesis and characterization of CdO-SnO2 NPs with excellent performance for Naphthol Blue Black (NBB) dye photodegradation and multi-application study. Materials Today: Proceedings, 67, 128–136.